Physicochemical properties and density functional theory calculation of octahedral UiO-66 with Bis (Trifluoromethanesulfonyl)imide ionic liquids

Mohd Faridzuan Majid [a,c], Hayyiratul Fatimah Mohd Zaid [b,c,*], Muhammad Fadhlullah Abd Shukur [a,c], Azizan Ahmad [d,e], Khairulazhar Jumbri [a,f]

[a] *Department of Fundamental and Applied Sciences, Universiti Teknologi PETRONAS, 32610, Seri Iskandar, Perak Darul Ridzuan, Malaysia*
[b] *Chemical Engineering Department, Universiti Teknologi PETRONAS, Seri Iskandar, 32610, Perak Darul Ridzuan, Malaysia*
[c] *Centre of Innovative Nanostructures & Nanodevices (COINN), Universiti Teknologi PETRONAS, 32610, Seri Iskandar, Perak Darul Ridzuan, Malaysia*
[d] *Department of Chemical Sciences, Universiti Kebangsaan Malaysia, Bangi, 43600, Selangor, Malaysia*
[e] *Department of Physics, Faculty of Science and Technology, Airlangga University (Campus C), Mulyorejo Road, Surabaya, 60115, Indonesia*
[f] *Centre for Research in Ionic Liquids (CORIL), Universiti Teknologi PETRONAS, 32610, Seri Iskandar, Perak Darul Ridzuan, Malaysia*

A R T I C L E   I N F O

A B S T R A C T

In this study, the physicochemical properties and molecular interactions between zirconium-based metal-organic framework (UiO-66) and three different ionic liquids based on bis(tri-fluoromethanesulfonyl)imide anion (EMIM$^+$, BMIM$^+$ and OMIM$^+$) was performed via a combined experimental and computational approach. The ionic liquid loaded UiO-66 or IL@UiO-66 was synthesized and characterized to understand the host-guest interaction. Density functional theory calculation was performed to analyse the electronic structure of IL@UiO-66 to provide molecular insight on the dominant interactions occurred in the hybrid material. Results showed that all ILs were successfully incorporated into the micropores of UiO-66. The 3D framework was retained even after loaded with ILs as analyzed from XRD pattern. FTIR spectrum reveals that interactions of ILs with UiO-66 influenced by the alkyl chain length of the cation. The anion has a profound affinity with the UiO-66 due to the presence of electronegative atoms. Phase transition study from DSC suggested that the incorporation of ILs has stabilized the framework of UiO-66 by shifting the endothermic peak to a higher state. These findings were further elaborated with DFT calculation. Geometrical optimizations confirmed the structural parameter changes of UiO-66 when loaded with ILs. These was mainly contributed by the non-covalent interactions which was confirmed by the reduced density gradient scattered plot. Another important findings are the strength of hydrogen bonding at the host-guest interface was influenced by the alkyl chain length. The molecular orbital analysis also shows that the size of alkyl chain influence the reactivity of the hybrid material. The present study provides fundamental insights on the molecular interaction of UiO-66 and ILs as a hybrid material, which can open new possibilities for advanced material for metal-organic framework applications in energy storage system, catalysis, gas storage and medicinal chemistry.

* Corresponding author. Chemical Engineering Department, Universiti Teknologi PETRONAS, Seri Iskandar, 32610, Perak Darul Ridzuan, Malaysia.
E-mail address: hayyiratul.mzaid@utp.edu.my (H.F. Mohd Zaid).

1. Introduction

Metal-organic framework (MOFs) have become a new trend in porous nanomaterials for various applications due to its unique microstructure and nanopores. The combination of inorganic metal nodes and organic linkers can produce a wide range of MOF which can be synthesized via solvothermal method, microwave-assisted method, mechanochemical, electrochemical synthesis, slow evaporation and diffusion method, microemulsion method, mixed solvent protocol, and many more [1–5]. Among the studied MOFs, the zirconium-based MOFs, namely the UiO-66 was one of the stable MOF which was made from $ZrO_6(OH)_4$ inorganic node and terephthalic acid as the organic linkers. Compared to other MOFs which has simpler repeating inorganic brick, the UiO-66 has a more complex structure due to the alternating tetrahedral and octahedral pore that are connected alternatively, making it difficult to be visualized without proper molecular visualization tool. However, because of the rigid framework of UiO-66, this MOF has an exceptional thermal and chemical stability, tunable pore size and high surface area. One of the unique characteristics of UiO-66 is its ability to form host-guest interactions with small guest molecules. Host-guest interactions are typically occurred in biological environment due to the lock and key *metaphor* and induced-fit characteristics of enzyme-protein complex. Inspired by the nature of chemical biology, host-guest interactions are possible in MOFs due to the void or nanopores that allow insertion of guest molecules, such as ionic liquids (ILs) [6] and small organic molecules like methanol or acetone, or even gases [7]. The host-guest interactions are important especially for separation and purification process such as water purification and gas separation and gas storage, drug delivery system for allowing efficient pharmacodynamics and pharmacokinetics of drug molecule onto the targeted organ and body system, chemical catalysis to increase selectivity, and activity for various chemical process, sensor application for detection of specific molecules and energy storage system that could provide fast charge transportation with high performance battery capacity.

A few studies suggested the enhanced activity of UiO-66 during host-guest interaction. For example, Sun et al. have developed advanced quasi-solid-state electrolyte based on the composite of UiO-66, polymers and ILs. They proposed that the immobilization of [EMIM][TFSI] IL increased the performance of fabricated lithium-ion battery thanks to the increased Li^+ transference number [8]. Yang et al. studied the performance of UiO-66 loaded with poly(ethylene oxide), PEO and lithium perchlorate, $LiClO_4$. Compared to the pristine structure, solid composite UiO-66 shows enhanced ionic conductivity and lithium transference number with higher electrochemical stability window. According to their thermal analysis via differential scanning calorimetry, the incorporation of PEO and $LiClO_4$ induced phase transition which shifted the melting temperature of the hybrid UiO-66 system [9]. Di et al. prepared amine-functionalized UiO-66 with poly(ILs) which was coated on carbon organic framework for radioactive waste management application. The core-shell like structure was able to remove as high as 80.4 % of ReO_4 from simulated waste model [10]. Iqbal et al. studied the promising application of UiO-66 loaded with IL for CO_2 separation. According to them, a hybrid UiO-66 and IL composite has a significant synergistic effect to increase CO_2 selectivity, which could be a valuable insight for carbon gas capture application [11]. Yin et al. synthesized UiO-66 loaded with Trihexyl(tetradecyl)phosphine bis(trifluoromethanesulfonyl)ammonia $[P_{6,6,6,14}]$ $[NTF_2]$ as efficient extractants and catalyst for extractive and catalytic-oxidative desulfurization of fuel oil. This material can remove sulphur as high as 95.3 % compared to pristine UiO-66 with 50.9 % efficiency. The synergistic effect of UiO-66 and $[P_{6,6,6,14}][NTF_2]$ could enhance the deep desulfurization of fuel oil, opening a new separation technology in fuel cleaning [12]. Wu et al. studied the encapsulation of ILs in amino-functionalized UiO-66 for enhance humidity sensing. They proposed that IL with similar size to UiO-66-NH_2 could be effectively incorporated into the micropore of MOF. They also verified that the response value of the humidity sensing test was correlated to the IL loading. The response values of the synthesized sensor was 221, higher than MOF utilizing MIL-125 (27.5) [13]. Chang et al. utilized IL@zwitterionic MOF for efficient separation of CO_2. The novel zwitterionic UiO-66 was synthesized via one-pot de novo method. Two organic linkers with different functional groups (amine and sulfonate) were mixed in a solvothermal reaction to form UiO-66 framework with cationic site of NH_3^+ and anionic site of SO_3^-. The IL was then incorporated by simple wet-impregnation method in ethanol solution. The performance of the IL@zwitterionic UiO-66 for CO_2 capture shows excellent enhancement (32–48 %) compared to single functionalized UiO-66. The separation selectivity of the CO_2 gas mixture also increased tremendously which was attributed to the full exposure of the active surface stie of ILs on the MOF [14]. Duan et al. reported the promising application of defected MOF for sewage separation. Compared to modulated-assisted synthesis of MOF and conventional utilization of N, N-dimethylformamide as solvent, the UiO-66-IL (IL: 1-ethyl-3-methylimidazolium acetate) shows increased adsorption performance for Rhodamine B (up to 7.652 mg g-1 at 39.85 °C). The reported porosity for the UiO-66-IL was very low, however the missing linker defects causing the MOF to produce more active sites, which can selectively adsorb the desire contaminant from sewage [15]. Cui et al. utilized 1-hexyl-3-methylimidazole tetrafluoroborate ($[HMIm]^+[BF_4]^-$@UiO-66) to solve the leaching of ILs caused by ion-exchange process in metal extraction application. The hybrid material shows excellent adsorption of Au(III) from electronic waste (284.64 mg g^{-1}) without significantly reduce the performance of the adsorbent [16].

The composite and the host-guest interactions of UiO-66 with ILs could improve the performance of targeted applications. The innovative design of such hybrid materials may open new possibilities of the usage and commercialization of UiO-66 soon. However, some questions are left unanswered, such as how the host-guest interactions of UiO-66 and ILs may occurred? The phase transition of IL loaded UiO-66 also leave us a question on why the incorporation of ILs lead to such transformations? The implementation of powerful material characterizations could provide a clue and insights on these research questions, but if these findings were tandem with the molecular perspective, we can clearly see the possible interactions and start to rethink the way we view the framework of UiO-66 itself. The molecular level understanding of UiO-66 can be analyzed via quantum chemical approach, namely the density functional theory (DFT) approach. The formalism uses a fundamental quantum mechanics equation that utilized Schrödinger equation to study the electronic properties of the material. When the electron density of materials is known, the electronic structure of model studied can be determined using post-processing DFT tool, such as the structural parameters, the molecular orbital analysis, the electrostatic potential

and topological analysis. Until now, the research papers that try to convey the electronic structure properties of UiO-66 are very limited [17–20]. By combining DFT calculation with experimental data, we can extract many useful finding which can facilitate us on the proper design of UiO-66 loaded with guest molecule such as ILs.

In this paper, the physicochemical properties of UiO-66 loaded with three bis(trifluoromethanesulfonyl)imide-based ILs with different alkyl chain length of cation was investigated. The choice of UiO-66 as the prototype MOF in this study stems from its established archetype in the field of MOF due to its rigid structure, tunable design and promising applications in various sectors. Utilizing UiO-66 as the prototype MOF can also reduce the resources expenditure due to its established solvothermal synthesis, making the research process more economical and reproducible [21–23]. The bis(trifluoromethanesulfonyl)imide anion is widely used in energy storage system and the study of their properties is needed [24,25]. The quantum insight of the UiO-66 and ILs were elucidated via DFT calculation to identify possible interactions that contribute to the host-guest interactions. These fundamental insights will provide future direction on the efficient design of hybrid IL@MOF in gas separation applications such as carbon dioxide capture with enhanced gas adsorption and selectivity. Moreover, the proper design of the hybrid material in battery component such as electrodes and electrolytes can be realized by understanding the ionic mechanism that could lead to high charge transport. On the other hand, the quantum understanding of IL@MOF can have several benefits for chemical catalysis in terms of the strategic enhancement of catalyst activity, improved selectivity, and prolonged stability for repeated use.

2. Research methodology

2.1. Chemicals

Zirconium(IV) chloride (98 %), $ZrCl_4$, and terephthalic acid (99+%) were purchased from Acros. 1-Ethyl-3-methylimidazolium bis (trifluoromethylsulfonyl)imide(98 %), [EMIM][TFSI] and 1-Butyl-3-methylimidazolium bis(trifluoromethylsulfonyl)imide (98 %), [BMIM][TFSI] was supplied by Sigma Aldrich. 1-Methyl-3-*n*-octylimidazolium bis(trifluoromethylsulfonyl)imide (99 %), [OMIM] [TFSI] was purchased from Alfa Aesar. Acetic acid glacial (100 %, anhydrous), acetone (ACS reagent) and *N, N*-Dimethylformamide, DMF were purchased from Merck. All chemicals were used without further purification step.

2.2. Synthesis of UiO-66@MOF and IL@UiO-66

The synthesis of UiO-66 was carried out using solvothermal synthesis method as described in other works [26–28]. 1.2 mmol of zirconium(IV) chloride, 1.2 mmol of terephthalic acid and 30 equivalents of acetic acid were transferred into reaction vial. The mixture was dissolved in 30 mL *N, N*-Dimethylformamide inside fume hood suction and swirled several times until all components are fully dissolved. Next, the vial was capped tight and transferred to a 120 °C pre-heated Memmert oven to initiate the crystallization process for 24 h. A yellowish cloudy mixture should be observed indicating the formation of UiO-66 inside DMF. The solvent was removed via centrifugation at 40000 rpm, and fresh DMF was used three times to eliminate the residues from the synthesis. The product was poured into a glass Petri dish and dried at 90 °C for 2 h in a vacuum oven before further use. The synthesis of IL@UiO-66 was done via
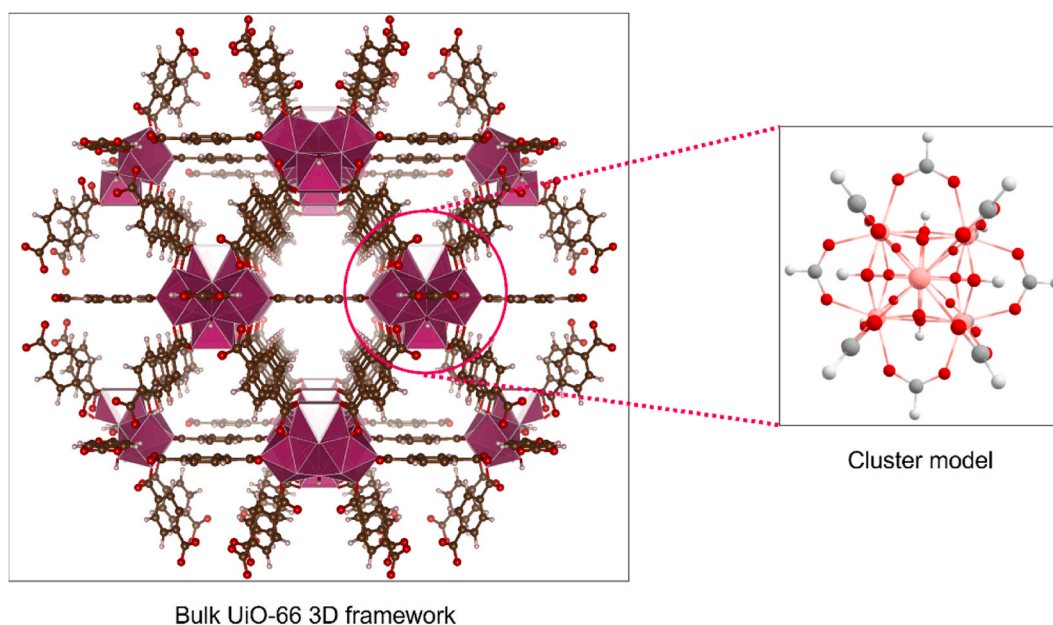

Fig. 1. The cluster model of UiO-66 was truncated from the bulk UiO-66 3D framework. The cluster model consists of zirconium metal node and terminated with 12 formates.

wet-impregnation method, where the dried MOF is added into the solution which contains the guest molecules [29]. The ILs were weighed according to the weight ratio of IL to UiO-66 of 0.35:0.65 and dissolved in 10 mL acetone in a vial. The solution was stirred for 15 min before added with UiO-66. The capped vial was continuously stirred overnight. Then, the acetone was allowed to be evaporated under fume hood suction. The sample was transferred to vacuum oven to allow complete drying at 80 °C for 2 h. The samples were labelled as IL@UiO-66, where IL were [EMIM][TFSI], [BMIM][TFSI] and [OMIM][TFSI].

2.3. Physicochemical characterizations

X-ray diffractograms of samples were characterized via Panalytical Xpert3 powder x-ray diffractometer (XRD), which used Cu Kα radiation (40 kV, 40 mA) and scanned at 2θ (2°–80°) with a rate of 4 °C per minute. The morphology of UiO-66 was analyzed using Zeiss Supra 55VP field emission scanning electron microscope (FESEM). The infrared spectrum of samples was obtained with Frontier 01 FTIR spectrometer by PerkinElmer at 64 scans with spectral resolution of 2 cm^{-1}. The heat flows of samples were analyzed using TA Instrument Q2000 differential scanning calorimeter (DSC).

2.4. DFT calculation methodology

Model cluster was used to perform DFT calculation of UiO-66. The CIF file of UiO-66 was downloaded from Crystallography Open Database and the file was modified using VESTA software [30]. The bulk structure was truncated to one inorganic brick which consists of 6 zirconium atoms coordinated with 12 formates terminating group as illustrated in Fig. 1. Such procedure was routinely used in model cluster truncation of UiO-66 for DFT calculation to save computational cost [18,19,31]. The geometry optimizations were performed for UiO-66 model cluster, individual ILs and IL@UiO-66 complex using ORCA (version 5.0.4) package [32]. The single point calculation was performed using the Lee, Yang, and Parr's (B3LYP) functional and def2-SVP basis set was implemented which uses the effective core potential (ECP) to replace the inner core electrons of heavy zirconium atom [33,34]. The geometry optimization level of theory utilized hybrid generalized gradient approximation (GGA), which is sufficient to study the non-covalent interactions in host-guest molecules [35]. The def2/J was used as the auxiliary basis. The output data of geometrical optimizations were visualized and analyzed using Chemcraft and Multiwfn post-processing tool [36,37].

3. Results and discussion

UiO-66 was synthesized via a solvothermal approach using DMF as a solvent and acetic acid as modulator. The repeating unit of UiO-66 was constructed from zirconium which were coordinated with 12 terephthalate linkers. Each of the metal clusters was bridged together that creates an alternating tetrahedral and octahedral pore. According to a few studies, the UiO-66 can exhibit a hydroxylated
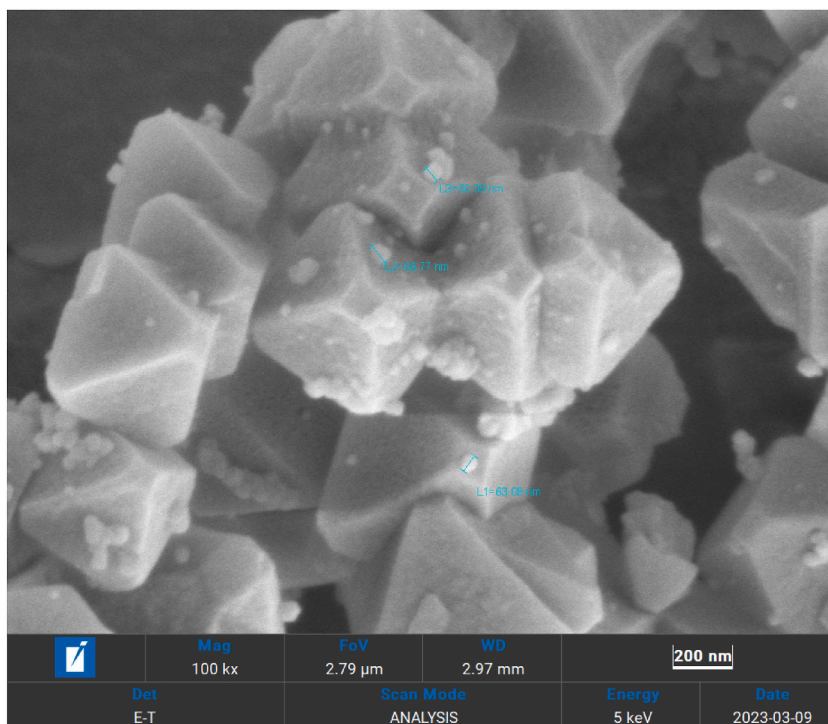

Fig. 2. The octahedral shape of UiO-66 can be clearly seen under field-emission SEM.

state where hydroxyl functional groups were connected with two neighbouring zirconium metals [20,38,39]. The morphology of UiO-66 exhibits a well-defined octahedral crystal shape as depicted in Fig. 2. The elemental mapping of UiO-66 via EDX mapping in Fig. 3 shows a good distribution of zirconium, carbon and oxygen with the weight percentage of 25.3 %, 52.1 % and 22.6 %, respectively. The dominating carbon elements signify the presence of terephthalate linkers, followed by zirconium nodes that were coordinated with oxygen atoms to form the metal cluster. XRD diffractogram of UiO-66 was visualized in Fig. 4. The intense sharp peaks can be clearly observed at $2\theta = 7.47°$ and $8.63°$, corresponding to the high crystallinity of UiO-66 from the (1 1 1) plane and (0 0 2) plane of the crystal structure, respectively. These planes describe the interplanar distance between octahedral pore and hexagonal channels. When loaded with ILs, the XRD patterns were retained with the decrease in the intensity of prominent peaks. These can be attributed to the appearance of an amorphous state, lattice strain or broadening due to the decrease in crystal size. In Fig. 5, the shift in XRD peaks to a lower angle suggests an increase in the d-spacing or interplanar distance of the UiO-66 structure. The incorporation of ILs into the micropore of UiO-66 induced a slight expansion of the crystal lattice. Moreover, the smaller peak intensity corresponds to a small reduction of crystallinity due to interactions of ILs. The different alkyl chain length of ILs may contribute to different peak size which depends on the strength of IL and UiO-66 interaction. However, the retention of the main XRD peaks signifies that the crystal structure remains largely intact upon IL loading.

The characteristic peaks of UiO-66 in FTIR spectra were visualized in Fig. 6 together with the IL-laden states. When compared side-by-side, the peak intensity was decreased which was attributed to the IL-occupied state on the surface sites of the UiO-66, which decrease the overall concentration of functional groups for infrared radiation. It was suggested that no new covalent bonds were formed, hence weak interactions might occur between ILs and UiO-66.

The peak shifts were studied by dividing the wavenumbers into three different regions, which were the organometallic region, the carboxylate region, and the aliphatic alkyl and hydroxyl region, which were depicted in Fig. S1, Fig. S2, and Fig. S3, respectively. The Zr–O bonds were indicated at 744 cm^{-1}. When ILs were loaded, the size of the peak got smaller, indicating that some of the ILs were interact with the Zr–O bond. The ILs peak such as the CF$_3$ antisymmetric bending and SOO antisymmetric bending was still retained in the IL@UiO-66 states. When comparing the size of the alkyl length, [EMIM][TFSI]@UiO-66 shows the smallest peak. This allowed [EMIM][TFSI] to be penetrated inside the UiO-66 micropores, allowing greater interaction with Zr–O, and thus the infrared signal is less detectable compared to [BMIM][TFSI] and [OMIM][TFSI]. The second intense peak at 660 cm^{-1} corresponds to the Zr$_6$(OH)$_4$O$_4$ cluster vibrations which usually do not shift [40]. Similar intensity reduction was also observed which indicates the infiltration of ILs inside the UiO-66 nanocages.

The interactions of IL and UiO-66 can also be interpreted from the carboxylate region. The carboxylate stretches were observed at 1390 cm^{-1} and 1670 cm^{-1}. The presence of IL may change the local electrical field and the bonding environment around the carboxylate groups. The slight blue shift at 1390 cm^{-1} suggested the interaction between cation species of ILs and terephthalate linker. Possible interactions could be the π-π stacking arose from the imidazolium ring of ILs and benzene ring of terephthalate linkers. The intensity of the terephthalate stretches also decreased as ILs were loaded into it due to the shielding effects arose from the MOF-IL
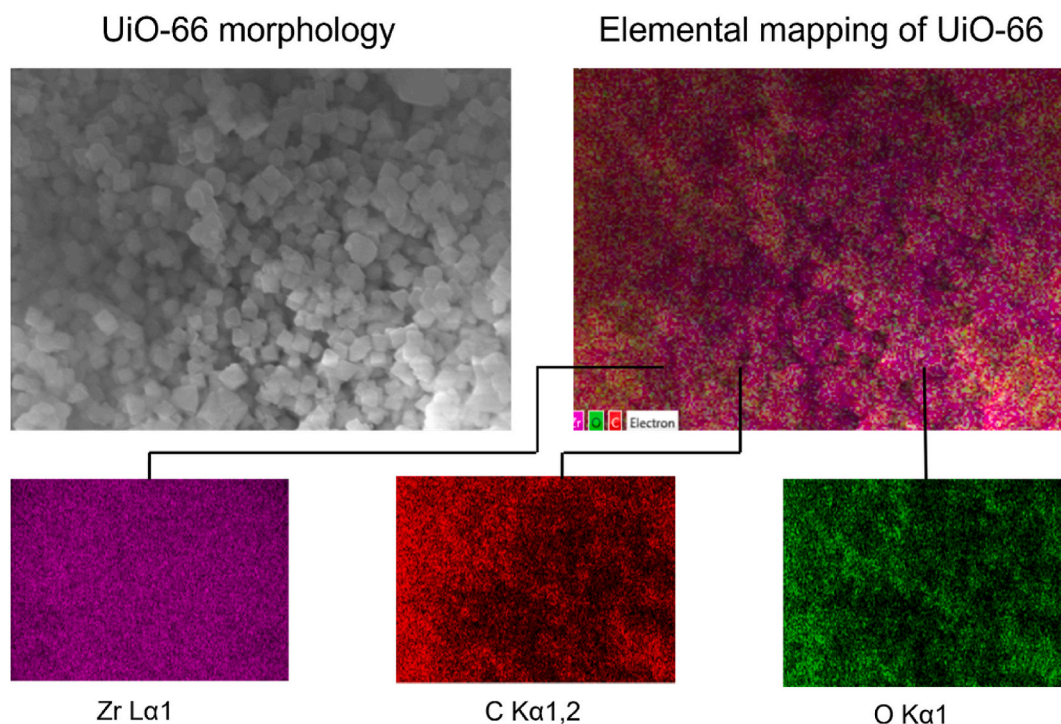

Fig. 3. The morphology of UiO-66 at 5 μm indicates a well distribution of zirconium, carbon and oxygen element.
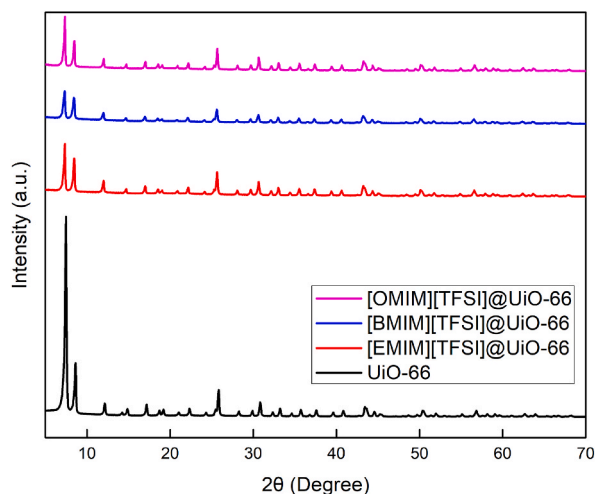
Fig. 4. XRD diffractograms of pristine UiO-66 and UiO-66 loaded with different alkyl chain of ionic liquids.
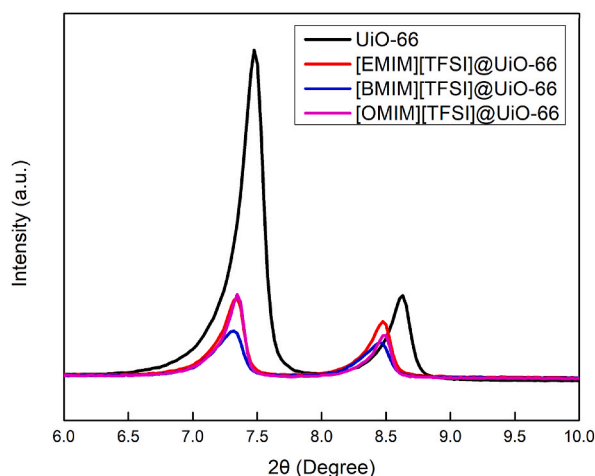

Fig. 5. The stacked XRD diffractograms of UiO-66 and their respective ionic liquids composite at 2θ from 6 to 10. These intense peaks belong to the octahedral micropore of UiO-66.

interactions. The intensity also decreased as the length of the alkyl chain of IL decreased. This was due to the conformational effects when ILs with different alkyl chain lengths can influence the conformational dynamics of the MOF framework. The shift of C=C phenyl vibration peaks to a higher wavenumber at IL@UiO-66 states indicate the presence of steric hindrance and electronic effects of the ILs on the terephthalate linkers. These may lead to aromatic ring distortion, which will eventually influence the C=C bond length and bond angle. The positively charged cation of ILs can also interact with the negatively charged terephthalate linker via electrostatic interactions. The two peaks located at 1330 cm^{-1} and 1347 cm^{-1} represent the fingerprints of neat ILs, specifically the N–C–H rocking from the imidazolium anions [41,42]. When loaded into UiO-66, the two peaks reduced in its intensity and flattening. The possible reason is the interaction and adsorption of the IL into the micropore of the UiO-66. However, the interaction is weak and not as strong as in the pure IL state. The absence of distinct new peaks characteristic of bond formation also suggests that there is no creation of new covalent bond. Moreover, the nanoconfinement effects could lead to these observations as the present of IL in the MOF's micropores can alter the changes in the molecular environment. The presence of the host molecule can also hinder the vibrational mode of the IL, leading to a reduced peak intensity and broadening. In Fig. S3, the condensed water in the framework of UiO-66 at 3100 cm^{-1} suggested the hydroxylated nature of the UiO-66 under study. The hydroxyl molecules can interact with terephthalate linkers through the formation of the hydrogen bond. When ILs were loaded, the hydroxylated nature of UiO-66 was slightly perturbed, and the physiosorbed water was displaced by the IL molecules, which decreases the hydroxyl stretching vibrations. The very small peak at 3650 cm^{-1} suggested the presence of an isolated surface hydroxyl groups which do not involve in hydrogen bonding with water molecules. The peak between 2800 and 3000 cm^{-1} corresponds to the stretching vibration of the CH alkyl chains of the cationic components of IL. Again, when UiO-66 was loaded with IL, the intensity of this alkyl peak decreased. The [EMIM][TFSI] shows the smallest peak, followed by [BMIM][TFSI] and [OMIM][TFSI]. It was suspected that the higher alkyl chain of [OMIM][TFSI] restricts
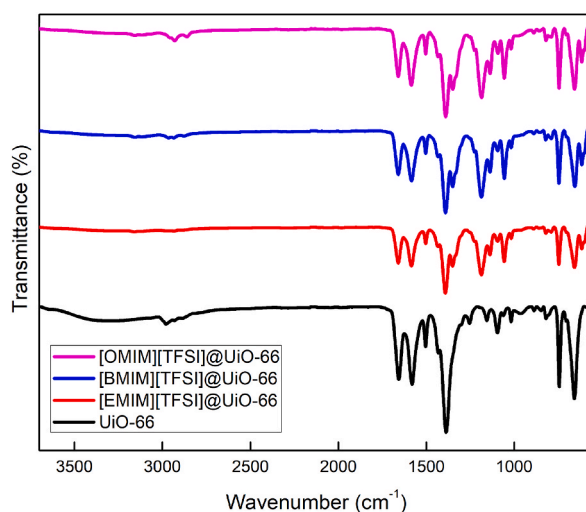
Fig. 6. The FTIR spectrum of UiO-66 and UiO-66 loaded with different alkyl chain of ionic liquids.

the insertion of this IL into the UiO-66, allowing more chain to be radiated with infrared. Additionally, the smaller size of [EMIM] [TFSI] and [BMIM][TFSI] allows them to be penetrated and interact with the framework, causing a blueshift in the CH peak. When IL interacts strongly with its environment, it experienced a change in vibrational energy levels, making it vibrates at a higher frequency.

To further analyse the behaviour of UiO-66 when loaded with ILs, DSC analysis was performed for UiO-66 and IL@UiO-66 states. The cyclic DSC measurement was set with 3 cycles of the heating-cooling-heating procedure. The first heating of the DSC curve was visualized in Fig. S4. The downward curves represent the loss of heat flow due to endothermic process such as phase transitions. For [EMIM][TFSI]@UiO-66 and [OMIM][TFSI]@UiO-66, the peaks were difficult to see, while the small peaks can be seen from [BMIM] [TFSI]@UiO-66 at 100–120 °C. These may suggest that the IL may stabilize the framework structure of UiO-66. In Fig. S5, downward spikes observed during the cooling process for [OMIM][TFSI]@UiO-66 between 110 and 120 °C suggest a phase transition occurred. Possible transitions were a new crystalline phase or the reordering of the framework structure during cooling. The absence of spikes for [BMIM][TFSI]@UiO-66 and [EMIM][TFSI]@UiO-66 may suggest non-significant structural changes upon cooling. One hypothesis is that a longer alkyl chains in [OMIM][TFSI] may aggregate on the surface of the UiO-66 which allows some of the ILs to undergo a phase transition. A similar study with different MOFs also hypothesizes that the excess ILs outside the cages of MOF explain why they were no peaks during the freezing process [43]. In Fig. S6, the upward peak during the second heating for UiO-66 could be due to melting or desolvation, which occurred during the cooling process. The absence of the features in the IL@UiO-66 states again may suggest that the incorporation of ILs could stabilize the framework and can modify the thermal characteristics of the hybrid material.

To shed light on the mechanisms of the interaction between UiO-66 and ILs, DFT calculation was performed for the UiO-66 using the cluster model approach. The accuracy and validity of the DFT result have been compared with experimental data from the existing literature. The detailed bond length was tabulated in Table S1 in the Supplementary Information. Selected structural parameters of the optimized UiO-66, ILs, and IL@UiO-66 were tabulated in Table 1, Table 2, and Table 3. By comparing the changes in the bond distance and bond angle of the studied model, a molecular insight could be generated to understand the most prominent interaction that occurs between the host and guest molecule. When IL was incorporated into the UiO-66 cluster, the Zr–O bond distance was decreased, while the neighbouring O–H distance was elongated, which suggested interaction has occurred upon confinement of IL. This was also confirmed from the blue shift observed at the Zr–O mode in Fig. S1. The pristine UiO-66 has a Zr–O mode at 744 cm^{-1}, and when ILs

Table 1

Parameters of optimized geometry of UiO-66 and [EMIM][TFSI]@UiO-66.

Parameters	UiO-66	[EMIM] [TFSI]	[EMIM][TFSI]@UiO-66
d(Zr–O)	2.27402$^{(Zr1\_O19)}$, 2.27481$^{(Zr2\_O19)}$, 2.27403$^{(Zr5\_O19)}$		2.26072$^{(Zr1\_O19)}$, 2.25165$^{(Zr2\_O19)}$, 2.26852$^{(Zr5\_O19)}$
d(O–H)	0.964		0.977
d(C–H imidazole)		1.08611	1.08600
d(C–H–N (anion))		2.76903	2.95958
d(C–F)		1.32728	1.32778
d(S–O)		1.45826	1.47038
a(Zr–O–H)	115.761$^{(Zr1\_O19\_H1)}$, 115.784$^{(Zr2\_O19\_H1)}$, 115.740$^{(Zr5\_O19\_H1)}$		116.080$^{(Zr1\_O19\_H1)}$, 114.819$^{(Zr2\_O19\_H1)}$, 115.984$^{(Zr5\_O19\_H1)}$
a(Zr–O–C)	133.097$^{(Zr1\_O2\_C2)}$, 133.183$^{(Zr2\_O15\_C2)}$		133.118$^{(Zr1\_O2\_C2)}$, 132.474$^{(Zr2\_O15\_C2)}$

Table 2
Parameters of optimized geometry of UiO-66 and [BMIM][TFSI]@UiO-66.

Parameters	UiO-66	[BMIM][TFSI]	[BMIM][TFSI]@UiO-66
d(Zr–O)	2.27402$^{(Zr1\_O19)}$, 2.27481$^{(Zr2\_O19)}$, 2.27403$^{(Zr5\_O19)}$		2.25588$^{(Zr1\_O19)}$, 2.25283$^{(Zr2\_O19)}$, 2.26184$^{(Zr5\_O19)}$
d(O–H)	0.964		0.97663
d(C–H imidazole)		1.08589	1.10323
d(C–H–N (anion))		2.79388	1.88998
d(C–F)		1.32736	1.32811
d(S–O)		1.45819	1.46730
a(Zr–O–H)	115.761$^{(Zr1\_O19\_H1)}$, 115.784$^{(Zr2\_O19\_H1)}$, 115.740$^{(Zr5\_O19\_H1)}$		116.075$^{(Zr1\_O19\_H1)}$, 114.802$^{(Zr2\_O19\_H1)}$, 115.570$^{(Zr5\_O19\_H1)}$
a(Zr–O–C)	133.097$^{(Zr1\_O2\_C2)}$, 133.183$^{(Zr2\_O15\_C2)}$		132.949$^{(Zr1\_O2\_C2)}$, 133.270$^{(Zr2\_O15\_C2)}$

Table 3
Parameters of optimized geometry of UiO-66 and [OMIM][TFSI]@UiO-66.

Parameters	UiO-66	[OMIM][TFSI]	[OMIM][TFSI]@UiO-66
d(Zr–O)	2.27397$^{(Zr1\_O20)}$, 2.27480$^{(Zr3\_O20)}$, 2.27419$^{(Zr4\_O20)}$		2.26050$^{(Zr1\_O20)}$, 2.26115$^{(Zr3\_O20)}$, 2.23186$^{(Zr4\_O20)}$
d(O–H)	0.96406		0.98351
d(C–H imidazole)		1.08598	1.08992
d(C–H–N (anion))		2.76845	2.00501
d(C–F)		1.32716	1.33109
d(S–O)		1.47659	1.47920
a(Zr–O–H)	115.756$^{(Zr1\_O20\_H2)}$, 115.794$^{(Zr3\_O20\_H2)}$, 115.731$^{(Zr4\_O20\_H2)}$		114.868$^{(Zr1\_O20\_H2)}$, 115.892$^{(Zr3\_O20\_H2)}$, 115.915$^{(Zr4\_O20\_H2)}$
a(Zr–O–C)	133.102$^{(Zr1\_O1\_C1)}$, 133.178$^{(Zr3\_O16\_C1)}$		133.404$^{(Zr1\_O1\_C1)}$, 133.236$^{(Zr3\_O16\_C1)}$

were incorporated, the wavenumber shift to 747 cm^{-1}, 746 cm^{-1}, and 745 cm^{-1} which corresponds to [EMIM][TFSI], [BMIM][TFSI], and [OMIM][TFSI], respectively. The shifting indicated a contraction of the Zr–O bond where the bond strength increased. Because of the strain effect of the framework, the Zr–O–H and Zr–O–C also show slight distortion. These intermolecular forces were due to the incoming of more electronegative IL, specifically the anion part as it contains fluorine, sulphur, and oxygen atoms. It was suspected that these atoms could also form hydrogen bonding to the surface of the UiO-66 framework. The blue shift spectrum of CF$_3$ bending, SNS bending, and SOO antisymmetric bending from the FTIR also confirm the strong interaction of ILs with the framework. For
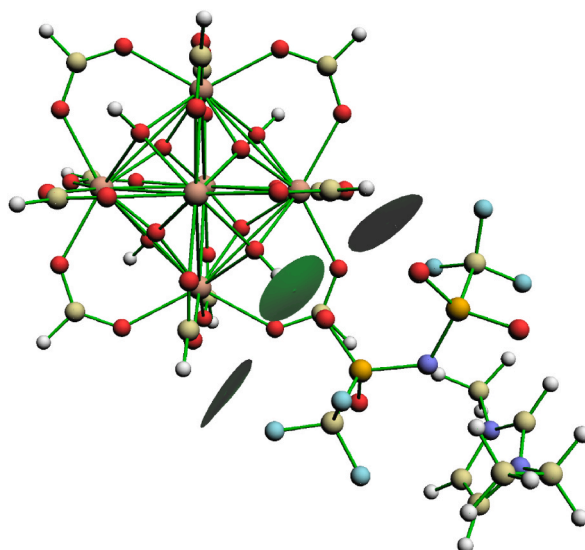

Fig. 7. Interbasin surfaces of [EMIM][TFSI]@UiO-66 generated from critical points of (3,-1) at the host-guest interface.

instance, the SNS stretching in [EMIM][TFSI], [BMIM][TFSI], and [OMIM][TFSI] at 650 cm^{-1}, 653 cm^{-1}, and 653 cm^{-1} were shifted to 657 cm^{-1}, 655 cm^{-1}, and 656 cm^{-1} when loaded into UiO-66. To investigate whether the host-guest interaction may change the cation-anion behaviour of ILs, the distance of C–H from the imidazole cation was recorded after geometry optimizations. For [BMIM] [TFSI]@UiO-66 and [OMIM][TFSI]@UiO-66, the increase in the bond distance from 1.08598 Å to 1.10323 Å and 1.08992 Å suggested an interaction of proton CH with the more electronegative nitrogen from the TFSI^{-} anion. As expected, the CH–N distance also decreased from 2.76845 Å to 1.88998 Å and 2.00501 Å for both [BMIM][TFSI]@UiO-66 and [OMIM][TFSI]@UiO-66, signifying the electron was pushed to the nitrogen. From the spectroscopic side, the bond elongations were confirmed from the hypsochromic shift at 3157 cm^{-1} to 3158 cm^{-1} for [BMIM][TFSI] and 3157 cm^{-1} to 3159 cm^{-1} for [OMIM][TFSI]. However, the distance of the CH–N bond in [EMIM][TFSI]@UiO-66 was increased to 2.95958 Å, as observed in the bathochromic shift from 3158 cm^{-1} to 3156 cm^{-1}, indicating that the anionic part of the IL has a great affinity towards UiO-66 cluster compared to its cation pair.

To elucidate the possible interactions that contribute to the host-guest interactions of UiO-66 and IL, the electron density and electrostatic potential were analyzed via topology analysis. Usually, the critical points or the bond critical point (BCP) were analyzed at (3, -1), which corresponds to the region in which the bond between two atoms is the strongest [44,45]. The BCP can also analyse the hydrogen bonding as part of the non-covalent interactions. The topology analysis of IL@UiO-66 was performed from the nuclear position as initial guesses first, followed by the midpoint of each two atoms. The BCP of [EMIM][TFSI]@UiO-66, [BMIM][TFSI] @UiO-66, and [OMIM][TFSI]@UiO-66 were shown in Fig. 7, Fig. 8, and Fig. 9, respectively. To locate the host-guest accessibility, the interbasin surfaces (IBS) were generated, which connect the atoms from IL and UiO-66. As can be seen from the figures, the IBS dissects the BCP pathway of the electronegative atoms from the anion site of IL to the hydrogen from the UiO-66 surface. 3 IBS could be generated for [EMIM][TFSI]@UiO-66, while the number of IBS for [BMIM][TFSI]@UiO-66 and [OMIM][TFSI]@UiO-66 was 5 and 7, respectively. The difference in IBS locations and the number of IBS were influenced by several factors, such as the orientation of ILs and the nature of IL itself. The high number of IBS in [OMIM][TFSI]@UiO-66 was due to the longer octyl chain of the cation site of IL. The presence of more carbon might participate in the intermolecular interactions, therefore some of the electron density in the host-guest interaction might be localized on the alkyl region. For [EMIM][TFSI]@UiO-66 and [BMIM][TFSI]@UiO-66, the main interactions came from the anionic part of the IL as the anion has block some of the electron density from being localized towards the UiO-66 cluster. The cluster model however has some limitation as it does not fully represent the periodic behaviour of the UiO-66 framework when impregnated with ILs. The octyl chain in [OMIM][TFSI] might have difficulty to passing through the UiO-66 channels, while shorter alkyl chain such as [EMIM][TFSI] and [BMIM][TFSI] could easily interact with the UiO-66.

From the IBS of IL@UiO-66, the strength of hydrogen bonding can also be evaluated. Emamian et al. proposed a method to calculate the hydrogen bond binding energy from the total electron density at BCP which belongs to hydrogen bonding [46]. The calculation of hydrogen bonding strength can be explained in (1):

$$BE \approx -223.08 \times \rho(rBCP) + 0.7423 \tag{1}$$

Where the BE is the hydrogen bond binding energy calculated in kcal/mol, and the ρ is in arbitrary unit (a.u.). This equation only applied for neutral hydrogen bonding. A summary of the BCP for all IL@UiO-66 states were tabulated in Table 4, where each BCP was corresponds to two atoms that could form hydrogen bonding. The optimized structure of all IL@MOF and the atomic labels were
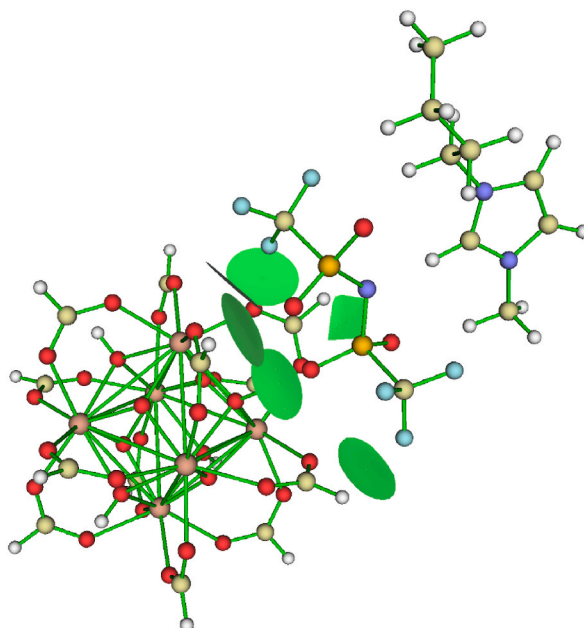

Fig. 8. Interbasin surfaces of [BMIM][TFSI]@UiO-66 generated from critical points of (3,-1) at the host-guest interface.
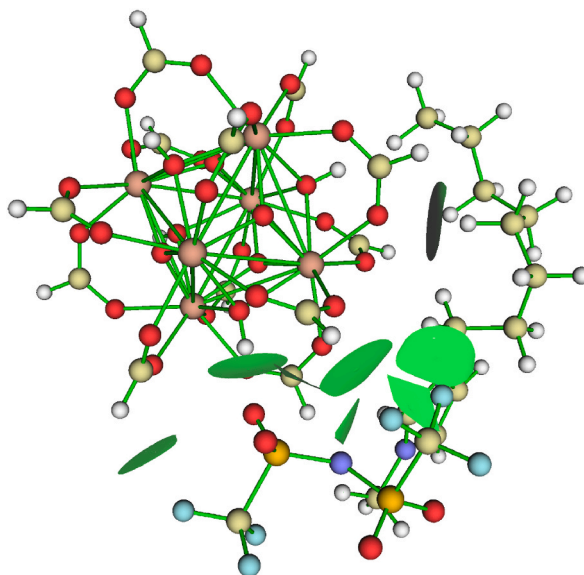
Fig. 9. Interbasin surfaces of [OMIM][TFSI]@UiO-66 generated from critical points of (3,-1) at the host-guest interface.

visualized in Fig. S7, Fig. S8, Fig. S9, Fig. S10, Fig. S11, and Fig. S12 in the Supplementary Information file. The most prominent hydrogen bonds were the O–H hydrogen bonds, where the oxygen atom came from the TFSI⁻ anion, and the hydrogen atom of the formate in UiO-66 cluster. [OMIM][TFSI]@UiO-66 has the highest hydrogen bond strength at O84–H7 (−8.3755 kcal/mol), followed by [BMIM][TFSI]@UiO-66 at O73–H6 (−6.9271 kcal/mol), and [EMIM][TFSI]@UiO-66 at O91–H6 (−6.4027 kcal/mol). The more negative the values of the binding energy, the greater the degree of interaction energy required to break the hydrogen bonds. The strong hydrogen bond in [OMIM][TFSI] can be explained by hydrophobic interactions between the octyl chain and the hydrophobic region of MOF. The neighbouring atoms can interact well as the alkyl chain moving towards the surface of UiO-66 [47]. These hydrogen bonds could be contributing to the host-guest interactions of IL and UiO-66 which also stabilizes the framework structure, as evidenced by the thermal analysis from DSC curves [48–50].

The presence of a different type of intermolecular forces in IL@UiO-66 can also be analyzed from the non-covalent interaction (NCI) method. NCI method identifies the region in a molecule where attractive and repulsive non-covalent interactions may occur. The NCI region was plotted as a reduced density gradient (RDG) value in a scattered map, where the blue and red colour corresponds to attractive and repulsive forces, respectively. The NCI scattered map of UiO-66 and all IL@UiO-66 states were illustrated in Fig. 10. As can be seen from the graph of UiO-66, the scattered points were mainly localized on the attractive forces and repulsive forces, which belong to hydrogen bonding and steric effect, respectively.

When IL was loaded, the grid points were now presence in the van der Waals interactions region in the middle of the graph with green color. This suggested that the incorporation of ILs may induce van der Waals forces. The intense spikes on the red region also become clearer, suggesting that repulsive forces were present. This might be because of IL itself, since bulky structures may trigger steric forces. The clear spike at the blue region of the scattered map also confirmed the enhanced hydrogen bonding thanks to the incoming electronegative atoms from ILs. These hydrogen bonds exist from the interaction between oxygen and hydrogen, fluorine and hydrogen, and nitrogen and hydrogen as evidence by the bond critical points calculated from the electron density topology analysis. The diminishing of isolated hydroxyl at 3700 cm⁻¹ for IL-loaded UiO-66 also confirms the existence of strong hydrogen bonding between IL and UiO-66. The use of the NCI method in UiO-66 was also investigated for gas adsorption and metal adsorption to provide insight on the role of non-covalent interactions [51,52].

The molecular orbital (MO) analysis of the UiO-66 and UiO-66 loaded with ILs was performed to indicate the electronic structure and to study the host-guest interaction. The different energy levels could provide molecular insight into the potential regions of interactions via orbital overlapping. The energy diagram for all IL@MOFs was illustrated in Fig. S7, Fig. S8, and Fig. S9, and the value of energy gaps were tabulated in Table 5. The energy gap of the [EMIM][TFSI]@UiO-66 was decreased from 6.020 eV to 5.656 eV, while for [BMIM][TFSI] and [OMIM][TFSI], the final energy gap was decreased to 5.420 eV and 5.991 eV, respectively. Decrease in the highest-occupied molecular orbital (HOMO) and lowest unoccupied molecular orbital (LUMO) signifying a stronger interaction between the IL and UiO-66 which resulted from the electronic states overlapping of the two molecules. The lower energy gap also corresponds to a more reactive host-guest state and favourable electron transfer, while the higher energy gap indicates that the material was less prone to a chemical reaction, a phenomena in which both electrons and nuclei undergo geometrical configurations and compositions transformation [53,54]. In host-guest system, the synergistic interaction might triggers consecutive chemical reactions of the MOF as well as changes in the physical properties. The possible chemical interactions were induced-fit or conformational selection which was like protein-ligand binding system [55,56]. In another study, a recognition first and reaction first mechanism were also suggested, but the finding was limited to crown system which contains cavity for the binding of small cations [57]. The decrease in

Table 4

Hydrogen bonding at the host-guest interface of UiO-66 and its respective ILs.

		Bond critical point index number	Atoms	Density of all electrons	Hydrogen bonding binding energy (kcal/mol)
MOF and IL interface	[EMIM][TFSI]@UiO-66	138	F95 – H30	0.0072	−0.8701
		183	O91 – H6	0.0320	−6.4027
		117	O86 – H28	0.0128	−2.1209
IL pair	[EMIM][TFSI]	106	O87 – H83	0.0089	−1.2336
		111	O87 – H80	0.0075	−0.9331
		129	O87 – H92	0.0117	−1.8669
		161	F98 – H92	0.0069	−0.7995
		202	F98 – H73	0.0072	−0.8669
		215	F100 – H77	0.0029	0.0901
		229	O90 – H77	0.0105	−1.5960
MOF and IL interface	[BMIM][TFSI]@UiO-66	110	F76 – H30	0.0062	−0.6487
		183	O73 – H6	0.0344	−6.9271
		139	O68 – H28	0.0118	−1.8871
		244	F81 – O22	0.0083	−1.1040
		224	F81 – O12	0.0071	−0.8320
		221	O72 – H25	0.0064	−0.6786
IL pair	[BMIM][TFSI]	156	N70 – H87	0.0351	−7.0896
		131	O69 – H103	0.0088	−1.2257
		162	O69 – H96	0.0109	−1.6922
		119	O69 – H100	0.0075	−0.9282
		199	F79 – H96	0.0068	−0.7811
		117	F75 – H92	0.0044	−0.2461
		164	O72 – H92	0.0187	−3.4358
MOF and IL interface	[OMIM][TFSI]@UiO-66	270	O83 – H31	0.0063	−0.6596
		326	O18 – H106	0.0150	−2.6069
		306	F93 – H31	0.0088	−1.2307
		186	F96 – H24	0.0029	0.0974
		230	O84 – H7	0.0409	−8.3755
		348	F91 – H80	0.0055	−0.4867
		335	F91 – H89	0.0059	−0.5715
		279	N67 – H29	0.0059	−0.5777
IL pair	[OMIM][TFSI]	346	O87 – H77	0.0094	−1.3495
		272	F95 – H75	0.0044	−0.2393
		290	N85 – H75	0.0110	−1.7205
		310	N85 – H89	0.0281	−5.5226
		335	F91 – H89	0.0059	−0.5715

HOMO-LUMO energy gap from [OMIM][TFSI]@UiO-66 to [EMIM][TFSI]@UiO-66 and further to [BMIM][TFSI]@UiO-66 suggests that the electronic structure of the materials was influenced by the length of alkyl chain in the cationic site of the IL. Although the trend might seem counterintuitive as why the [BMIM][TFSI]@UiO-66 has the least energy gap, a combination of other factors can influence the final energy calculated. The placement of the initial structure of the MOF-IL can cause such anomalies in the result which may alter the adsorption configuration, the orientation and distance between IL and MOF, the conformational effects and the charge redistribution. In this study, all ILs were placed near to the formate-terminated group of the UiO-66 model cluster. During optimization calculation, the coordinates of all atoms may undergo distortions that can have cascading effects on the overall electronic structure and energy levels. On the other hand, the conformational flexibility of the ILs may contribute to different degrees of interactions with UiO-66 which can influence the final energy of the system. Recent study shows that the molecular mobility of a system was influenced by viscosity of the ILs [58]. The viscosity of [EMIM][TFSI], [BMIM][TFSI], and [OMIM][TFSI] were 139×10^5 mPas, 125×10^5 mPas, and 385×10^5 mPas, respectively. These values were extracted from the fit parameters study of the viscosity of room temperature ILs using the Cohen-Turnbull equation [59,60]. Longer alkyl chain IL like [OMIM][TFSI] has larger steric hindrance when being introduced to UiO-66, which could affect the molecular packing within the IL structure. The bulky effect of the octyl chain may hinder the electronic overlap between molecules, which results in higher energy gap [61,62]. Moreover, the octyl chain can reduce the electrostatic interaction strength between the charged species, causing electronic structure and energy levels disruptions.

The electron density difference of IL@UiO-66 can be determined by subtracting the total electron density of the IL and pristine UiO-66 from their IL@UiO-66 complex state. This analysis can reveal if there is an electron accumulation or depletion, which may provide perspective on the nature of interaction between the host-guest system. The contour maps of difference density for all IL@UiO-66 were depicted in Fig. S10, Fig. S11, and Fig. S12. The atoms involved for the generation of contour map was picked between three atoms that connects the host-guest interface of the model studied. The normal line and dashed line indicate the region that has increased electron density and reduced electron density, respectively. When [EMIM][TFSI] was loaded into the UiO-66, the electron density localized on the region between Zr–H and O–O from the UiO-66. The dashed line was prominent at the host-guest interface, suggesting that the
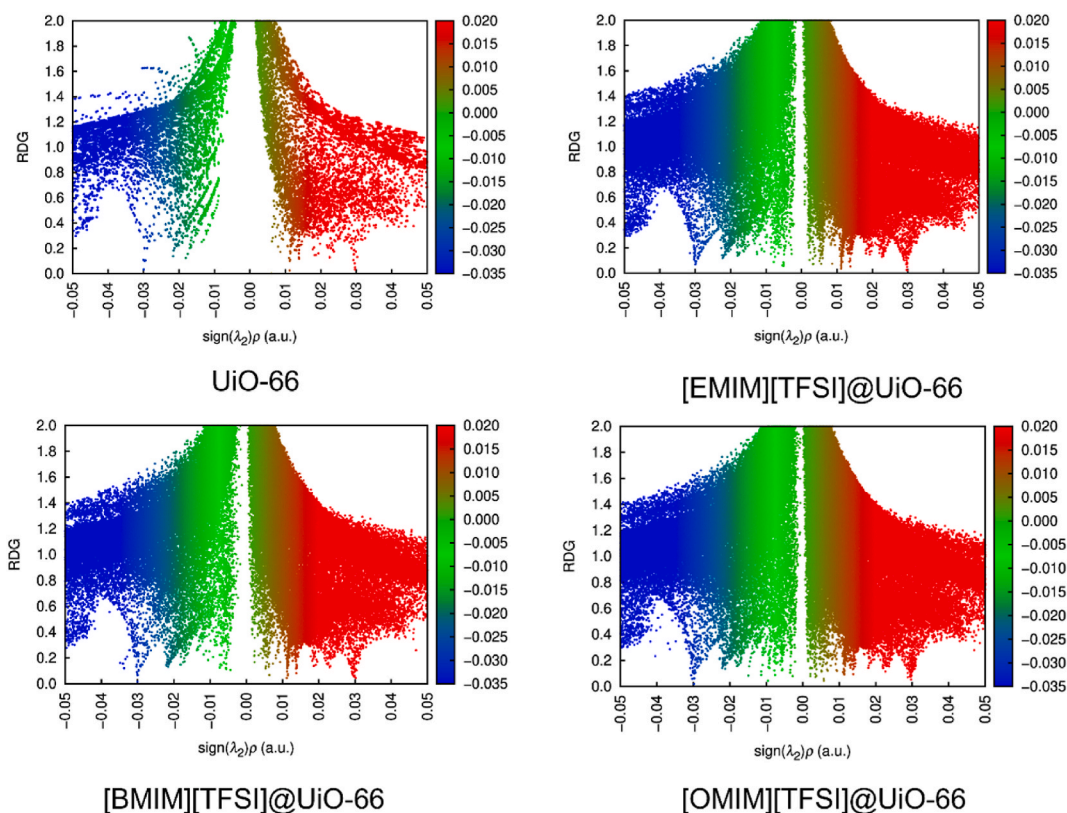
Fig. 10. Scatter graph on non-covalent interactions of UiO-66 and UiO-66 loaded with different alkyl chain of ILs. The scatters are analyzed from the grid point in 3D space.

Table 5
Highest occupied molecular orbital (HOMO) and lowest unoccupied molecular orbital (LUMO) of UiO-66 and IL@UiO-66.

	Highest occupied molecular orbital (HOMO) (eV)	Lowest unoccupied molecular orbital (LUMO) (eV)	HOMO-LUMO gap (eV)
UiO-66	−7.670854	−1.650544	6.020311
[EMIM] [TFSI] @UiO-66	−7.130105	−1.473315	5.656789
[BMIM] [TFSI] @UiO-66	−7.064430	−1.644166	5.420264
[OMIM] [TFSI] @UiO-66	−7.514551	−1.522757	5.991794

electron-withdrawing effect from the electronegative atoms [63,64]. Meanwhile, the electron density was increased at the interface of host-guest region in [BMIM][TFSI]@UiO-66 and [OMIM][TFSI]@UiO-66. Several factors that could contribute to this anomalies were the different size of alkyl chain of cation of IL, different orientation of IL and anion configuration. Because of the smaller size of [EMIM] [TFSI], it has strong affinity to UiO-66, leading to more significant perturbation of electron density compared to [BMIM][TFSI] and [OMIM][TFSI]. Moreover, the shape of EMIM$^+$ cation was more planar compared to BMIM$^+$ and OMIM$^+$, which can have a larger orbital overlap and resulting in pronounced changes in electron density [65].

4. Conclusions

Based on the physicochemical properties, it can be concluded that the UiO-66 has been successfully synthesized where the ILs with different alkyl chains (EMIM$^+$, BMIM$^+$, OMIM$^+$) were effactually incorporated into the micropores of UiO-66. The DFT analysis and post-topology analysis revealed that the host-guest interactions between UiO-66 and ILs were predominantly non-covalent, with the most contribution coming from hydrogen bonding between the oxygen atom of bis(trifluoromethanesulfonyl)imide anion and the hydrogen from the formate terminating group in UiO-66 model cluster. The electron density difference analysis manifest increased electron density at the host-guest interface. The smaller HOMO-LUMO energy gap in [EMIM][TFSI]@UiO-66 and [BMIM][TFSI] @UiO-66 compared to larger gap in [OMIM][TFSI]@UiO-66 shows how the alkyl chain length can influence the reactivity of the material. Some of the findings from DFT calculation were confirmed from the experimentally characterized material such as the FTIR peak shifting and the absence of endothermic peak in DSC. Although these findings are specific to UiO-66 MOF, there is a potential

applicability to other types of MOF especially MOFs with similar microporous architectures and morphology such as UiO-67 and UiO-68, where the only difference in comparison with the current study is the length of the organic linker. Other types of MOF are also worth to explore such as HKUST-1, MOF-5, MIL-101 and NU-1000. The physicochemical properties and electronic structure study of these MOFs could confirm the generality of the findings and provide a broader insights on the host-guest interactions between MOF and ILs. Overall, this study provides future direction on the design of hybrid nanomaterials for various application, especially in the development of catalyst, energy storage device, gas capture and drug-delivery system.

CRediT authorship contribution statement

Mohd Faridzuan Majid: Writing – original draft, Visualization, Software, Methodology, Investigation, Formal analysis, Data curation, Conceptualization. **Hayyiratul Fatimah Mohd Zaid:** Writing – review & editing, Validation, Supervision, Resources, Project administration, Funding acquisition, Conceptualization. **Muhammad Fadhlullah Abd Shukur:** Supervision, Resources, Methodology. **Azizan Ahmad:** Writing – review & editing, Supervision, Project administration, Conceptualization. **Khairulazhar Jumbri:** Validation, Software, Methodology.

Declaration of competing interest

The authors declare the following financial interests/personal relationships which may be considered as potential competing interests:Hayyiratul Fatimah Mohd Zaid reports financial support was provided by UTP Foundation.

Acknowledgements

Appendix A. Supplementary data

Supplementary data to this article can be found online at https://doi.org/10.1016/j.heliyon.2023.e20743.

References

[1] Y. Yao, X. Zhao, G. Chang, X. Yang, B. Chen, Hierarchically porous metal–organic frameworks: synthetic strategies and applications, Small Structures 4 (1) (Jan. 2023), 2200187, https://doi.org/10.1002/sstr.202200187.
[2] H. Xiao, Z.-X. Low, D.B. Gore, R. Kumar, M. Asadnia, Z. Zhong, Porous metal–organic framework-based filters: synthesis methods and applications for environmental remediation, Chem. Eng. J. 430 (Feb. 2022), 133160, https://doi.org/10.1016/j.cej.2021.133160.
[3] N. Stock, S. Biswas, Synthesis of metal-organic frameworks (MOFs): routes to various MOF topologies, morphologies, and composites, Chem. Rev. 112 (2) (2012) 933–969, https://doi.org/10.1021/cr200304e. Feb.
[4] J. Annamalai, et al., Synthesis of various dimensional metal organic frameworks (MOFs) and their hybrid composites for emerging applications – a review, Chemosphere 298 (2022), 134184, https://doi.org/10.1016/j.chemosphere.2022.134184. Jul.
[5] J. Guo, et al., The biomimetic engineering of metal–organic frameworks with single-chiral-site precision for asymmetric hydrogenation, J. Mater. Chem. A 10 (12) (2022) 6463–6469, https://doi.org/10.1039/D1TA08319H.
[6] Y. Li, et al., Highly efficient triiodide ion adsorption from water by ionic liquid hybrid metal–organic frameworks, J. Mol. Liq. 370 (Jan. 2023), 121009, https://doi.org/10.1016/j.molliq.2022.121009.
[7] S.K. Gupta, A.K. Gupta, R.K. Yadav, Theoretical studies of physical, chemical, and vibrational properties of various imidazolium-based ionic liquids, Acta Phys. Pol. 140 (5) (Nov. 2021) 400–406, https://doi.org/10.12693/APhysPolA.140.400.
[8] M. Sun, et al., Fast Li+ transport pathways of quasi-solid-state electrolyte constructed by 3D MOF composite nanofibrous network for dendrite-free lithium metal battery, Mater. Today Energy 29 (2022), 101117, https://doi.org/10.1016/j.mtener.2022.101117. Oct.
[9] J. Yang, et al., Effect of intermolecular interactions on the performance of UiO-66-laden solid composite polymer electrolytes, J. Alloys Compd. 845 (2020), 155179, https://doi.org/10.1016/j.jallcom.2020.155179. Dec.
[10] Z. Di, Z.-F. Liu, H.-R. Li, Z. Liu, C.-P. Li, Enhancing the stability of poly(ionic liquids)@MOFs@COFs via core–shell protection strategy for [99] TcO [4] [−] sequestration, Inorg. Chem. Front. 10 (3) (2023) 952–958, https://doi.org/10.1039/D2QI02147A.
[11] Z. Iqbal, et al., One pot synthesis of UiO-66@IL composite for fabrication of CO2 selective mixed matrix membranes, Chemosphere 303 (Sep. 2022), 135122, https://doi.org/10.1016/j.chemosphere.2022.135122.
[12] J. Yin, et al., UiO-66(Zr)-based porous ionic liquids for highly efficient extraction coupled catalytic oxidative desulfurization, Chem. Eng. J. 470 (Aug. 2023), 144290, https://doi.org/10.1016/j.cej.2023.144290.
[13] K. Wu, X. Miao, H. Zhao, S. Liu, T. Fei, T. Zhang, Selective encapsulation of ionic liquids in UiO-66-NH $_2$ nanopores for enhanced humidity sensing, ACS Appl. Nano Mater. 6 (10) (May 2023) 9050–9058, https://doi.org/10.1021/acsanm.3c01727.
[14] Y. Chang, et al., Zwitterionic metal–organic framework with highly dispersed ionic liquid for enhancing CO2 capture, Sep. Purif. Technol. 326 (Dec. 2023), 124828, https://doi.org/10.1016/j.seppur.2023.124828.
[15] J.-J. Duan, et al., Regulating defected zirconium metal–organic frameworks in ionic liquid for sewage treatment, J. Mol. Struct. 1286 (Aug. 2023), 135607, https://doi.org/10.1016/j.molstruc.2023.135607.
[16] X. Cui, Y. Wang, Y. Wang, P. Zhang, W. Lu, Extraction of gold based on ionic liquid immobilized in UiO-66: an efficient and reusable way to avoid IL loss caused by ion exchange in solvent extraction, Molecules 28 (5) (Feb. 2023) 2165, https://doi.org/10.3390/molecules28052165.
[17] M. Janani, M. Prakash, Screening of suitable size/pore dependent IL/UiO-66 composite for selective gas separation application, ECS Trans. 107 (1) (Apr. 2022) 13625–13635, https://doi.org/10.1149/10701.13625ecst.

[18] R. Stanton, D.J. Trivedi, Influence of defects and linker exchange on removal of phosphate using MOFs with the node structure $M_6(OH)_4(O)_4$ for M = Hf, Zr, or Ce, Chem. Mater. 33 (14) (Jul. 2021) 5730–5737, https://doi.org/10.1021/acs.chemmater.1c01521.

[19] A. Nandy, A.C. Forse, V.J. Witherspoon, J.A. Reimer, NMR spectroscopy reveals adsorbate binding sites in the metal–organic framework UiO-66(Zr), J. Phys. Chem. C 122 (15) (Apr. 2018) 8295–8305, https://doi.org/10.1021/acs.jpcc.7b12628.

[20] C.S. Cox, V. Cossich Galicia, M. Lessio, Computational insights into as(V) removal from water by the UiO-66 metal–organic framework, J. Phys. Chem. C 125 (5) (Feb. 2021) 3157–3168, https://doi.org/10.1021/acs.jpcc.0c09465.

[21] S. Bae, N. Zaini, K.S.N. Kamarudin, K.S. Yoo, J. Kim, M.R. Othman, Rapid solvothermal synthesis of microporous UiO-66 particles for carbon dioxide capture, Kor. J. Chem. Eng. 35 (3) (2018) 764–769, https://doi.org/10.1007/s11814-017-0334-4. Mar.

[22] L.A. Lozano, C.M. Iglesias, B.M.C. Faroldi, M.A. Ulla, J.M. Zamaro, Efficient solvothermal synthesis of highly porous UiO-66 nanocrystals in dimethylformamide-free media, J. Mater. Sci. 53 (2018) 1862–1873, https://doi.org/10.1007/s10853-017-1658-5. Feb.

[23] X. Liu, N.K. Demir, Z. Wu, K. Li, Highly water-stable zirconium metal–organic framework UiO-66 membranes supported on alumina hollow fibers for desalination, J. Am. Chem. Soc. 137 (22) (Jun. 2015) 6999–7002, https://doi.org/10.1021/jacs.5b02276.

[24] T. Placke, et al., In situ X-ray diffraction studies of cation and anion intercalation into graphitic carbons for electrochemical energy storage applications: in situ X-ray diffraction studies for electrochemical energy storage applications, Z. Anorg. Allg. Chem. 640 (10) (2014) 1996–2006, https://doi.org/10.1002/zaac.201400181. Aug.

[25] Z. Huang, X. Li, Z. Chen, P. Li, X. Ji, C. Zhi, Anion chemistry in energy storage devices, Nat Rev Chem, Jun. (2023), https://doi.org/10.1038/s41570-023-00506-w.

[26] Mohd F. Majid, H.F. Mohd Zaid, M.F. Abd Shukur, A. Ahmad, K. Jumbri, Host–guest interactions of zirconium-based metal–organic framework with ionic liquid, Molecules 28 (6) (Mar. 2023) 2833, https://doi.org/10.3390/molecules28062833.

[27] P. Chen, S. Liu, Z. Bai, Y. Liu, Enhanced ionic conductivity of ionic liquid confined in UiO-67 membrane at low humidity, Microporous Mesoporous Mater. 305 (2020), 110369–110369.

[28] V. Nozari, C. Calahoo, J.M. Tuffnell, D.A. Keen, T.D. Bennett, L. Wondraczek, Ionic liquid facilitated melting of the metal-organic framework ZIF-8, Nat. Commun. 12 (1) (2021), https://doi.org/10.1038/s41467-021-25970-0, 5703, Dec.

[29] J. Guo, Y. Wan, Y. Zhu, M. Zhao, Z. Tang, Advanced photocatalysts based on metal nanoparticle/metal-organic framework composites, Nano Res. 14 (7) (2021) 2037–2052, https://doi.org/10.1007/s12274-020-3182-1. Jul.

[30] S. Øien, et al., Detailed structure analysis of atomic positions and defects in zirconium metal–organic frameworks, Cryst. Growth Des. 14 (11) (2014) 5370–5372, https://doi.org/10.1021/cg501386j. Nov.

[31] B. Yeh, et al., Site densities, rates, and mechanism of stable Ni/UiO-66 ethylene oligomerization catalysts, J. Am. Chem. Soc. 143 (48) (2021) 20274–20280, https://doi.org/10.1021/jacs.1c09320. Dec.

[32] F. Neese, Software update: the ORCA program system—version 5.0, WIREs Comput Mol Sci 12 (5) (2022), https://doi.org/10.1002/wcms.1606.

[33] X. Xu, D.G. Truhlar, Accuracy of effective core potentials and basis sets for density functional calculations, including relativistic effects, as illustrated by calculations on arsenic compounds, J. Chem. Theor. Comput. 7 (9) (Sep. 2011) 2766–2779, https://doi.org/10.1021/ct200234r.

[34] M.N. Vo, J.P. Ruffley, J.K. Johnson, Impact of defects on the decomposition of chemical warfare agent simulants in Zr-based metal organic frameworks, AIChE J. 67 (3) (2021), https://doi.org/10.1002/aic.17156. Mar.

[35] F. Li, G. Zhang, S. Xia, L. Yu, Host-guest interactions accompanying the cationic nitrogen heterocyclic guests encapsulation within pillar[5]arene: a theoretical research, J. Mol. Struct. 1198 (Dec. 2019), 126862, https://doi.org/10.1016/j.molstruc.2019.07.109.

[36] T. Lu, F. Chen, Multiwfn: a multifunctional wavefunction analyzer, J. Comput. Chem. 33 (5) (Feb. 2012) 580–592, https://doi.org/10.1002/jcc.22885.

[37] T. Lu, Q. Chen, Independent gradient model based on Hirshfeld partition: a new method for visual study of interactions in chemical systems, J. Comput. Chem. 43 (8) (Mar. 2022) 539–555, https://doi.org/10.1002/jcc.26812.

[38] S.M.J. Rogge, et al., Thermodynamic insight in the high-pressure behavior of UiO-66: effect of linker defects and linker expansion, Chem. Mater. 28 (16) (Aug. 2016) 5721–5732, https://doi.org/10.1021/acs.chemmater.6b01956.

[39] A.E. Khudozhitkov, S.S. Arzumanov, D.I. Kolokolov, A.G. Stepanov, Butane isomers mobility and framework dynamics in UiO-66 (Zr) MOF: impact of the hydroxyl groups in zirconia cluster, Solid State Nucl. Magn. Reson. 118 (Apr. 2022), 101784, https://doi.org/10.1016/j.ssnmr.2022.101784.

[40] V.V. Butova, et al., Loading of the model amino acid leucine in UiO-66 and UiO-66-NH$_2$: optimization of metal–organic framework carriers and evaluation of host–guest interactions, Inorg. Chem. 60 (8) (Apr. 2021) 5694–5703, https://doi.org/10.1021/acs.inorgchem.0c03751.

[41] N.R. Dhumal, M.P. Singh, J.A. Anderson, J. Kiefer, H.J. Kim, Molecular interactions of a Cu-based metal–organic framework with a confined imidazolium-based ionic liquid: a combined density functional theory and experimental vibrational spectroscopy study, J. Phys. Chem. C 120 (6) (2016), 3295-3304-3295–3304.

[42] Q. Huang, Q. Luo, Y. Wang, E. Pentzer, B. Gurkan, Hybrid ionic liquid capsules for rapid CO$_2$ capture, Ind. Eng. Chem. Res. 58 (24) (Jun. 2019) 10503–10509, https://doi.org/10.1021/acs.iecr.9b00314.

[43] K. Fujie, T. Yamada, R. Ikeda, H. Kitagawa, Introduction of an ionic liquid into the micropores of a metal–organic framework and its anomalous phase behavior, Angew. Chem. 126 (42) (2014), 11484–11487–11484–11487.

[44] X. Luo, et al., Host–guest chirality interplay: a mutually induced formation of a chiral zmof and its double-helix polymer guests, J. Am. Chem. Soc. 138 (3) (Jan. 2016) 786–789, https://doi.org/10.1021/jacs.5b12516.

[45] M.E. Beck, C. Riplinger, F. Neese, G. Bistoni, Unraveling individual host–guest interactions in molecular recognition from first principles quantum mechanics: insights into the nature of nicotinic acetylcholine receptor agonist binding, J. Comput. Chem. 42 (5) (Feb. 2021) 293–302, https://doi.org/10.1002/jcc.26454.

[46] S. Emamian, T. Lu, H. Kruse, H. Emamian, Exploring nature and predicting strength of hydrogen bonds: a correlation analysis between atoms-in-molecules descriptors, binding energies, and energy components of symmetry-adapted perturbation theory, J. Comput. Chem. 40 (32) (Dec. 2019) 2868–2881, https://doi.org/10.1002/jcc.26068.

[47] N. Zhang, et al., Confinement effect of ionic liquid: improve of the extraction performance of parent metal organic framework for phthalates, J. Chromatogr. A 1703 (Aug. 2023), 464101, https://doi.org/10.1016/j.chroma.2023.464101.

[48] M. Rojas-Poblete, P.L. Rodríguez-Kessler, R. Guajardo-Maturana, C. Olea Ulloa, A. Muñoz-Castro, Nature and role of formal charge of the ion inclusion in hexanuclear Platinum(II) Host-Guest Species. Insights from relativistic DFT calculations, Inorg. Chim. Acta 546 (Feb. 2023), 121298, https://doi.org/10.1016/j.ica.2022.121298.

[49] P. Shang, G. Dong, X.-F. Jiang, Hydrogen bonds promoted formation of Eu(III)-based host-guest complex and luminescence properties, Inorg. Chim. Acta 530 (Jan. 2022), 120676, https://doi.org/10.1016/j.ica.2021.120676.

[50] J. Zhang, W. Kosaka, Y. Kitagawa, H. Miyasaka, Host–guest hydrogen bonding varies the charge-state behavior of magnetic sponges, Angew. Chem. 131 (22) (May 2019) 7429–7434, https://doi.org/10.1002/ange.201902301.

[51] I. Walton, C. Chen, J.M. Rimsza, T.M. Nenoff, K.S. Walton, Enhanced sulfur dioxide adsorption in UiO-66 through crystal engineering and chalcogen bonding, Cryst. Growth Des. 20 (9) (Sep. 2020) 6139–6146, https://doi.org/10.1021/acs.cgd.0c00846.

[52] D. Santibañez, F. Mendizabal, Understanding lead and mercury adsorption by post-synthetically modified linkers in UiO-66 MOF. A computational theoretical study, Mol. Simulat. 49 (5) (Mar. 2023) 481–488, https://doi.org/10.1080/08927022.2023.2171073.

[53] M. Miar, A. Shiroudi, K. Pourshamsian, A.R. Oliaey, F. Hatamjafari, Theoretical investigations on the HOMO–LUMO gap and global reactivity descriptor studies, natural bond orbital, and nucleus-independent chemical shifts analyses of 3-phenylbenzo[*d*]thiazole-2(3 *H*)-imine and its *para* -substituted derivatives: solvent and substituent effects, J. Chem. Res. 45 (1–2) (Jan. 2021) 147–158, https://doi.org/10.1177/1747519820932091.

[54] D. Chen, H. Wang, HOMO-LUMO energy splitting in polycyclic aromatic hydrocarbons and their derivatives, Proc. Combust. Inst. 37 (1) (2019) 953–959, https://doi.org/10.1016/j.proci.2018.06.120.

[55] W. Chen, et al., Enhancing hit discovery in virtual screening through absolute protein–ligand binding free-energy calculations, J. Chem. Inf. Model. 63 (10) (May 2023) 3171–3185, https://doi.org/10.1021/acs.jcim.3c00013.

[56] J. Shi, J.-H. Cho, W. Hwang, Heterogeneous and allosteric role of surface hydration for protein–ligand binding, J. Chem. Theor. Comput. 19 (6) (Mar. 2023) 1875–1887, https://doi.org/10.1021/acs.jctc.2c00776.

[57] Y. Sakata, M. Tamiya, M. Okada, S. Akine, Switching of *recognition first* and *reaction first* mechanisms in host–guest binding associated with chemical reactions, J. Am. Chem. Soc. 141 (39) (Oct. 2019) 15597–15604, https://doi.org/10.1021/jacs.9b06926.

[58] F. Philippi, D. Pugh, D. Rauber, T. Welton, P.A. Hunt, Conformational design concepts for anions in ionic liquids, Chem. Sci. 11 (25) (2020) 6405–6422, https://doi.org/10.1039/D0SC01379J.

[59] D. Merunka, M. Peric, An analysis of radical diffusion in ionic liquids in terms of free volume theory, J. Chem. Phys. 152 (2) (Jan. 2020), 024502, https://doi.org/10.1063/1.5138130.

[60] A. Aminian, V. Vinš, Molecular simulations of transport properties of polar hydrofluoroethers: force field development, fractional Stokes-Einstein and free volume relations, J. Mol. Liq. 389 (Nov. 2023), 122847, https://doi.org/10.1016/j.molliq.2023.122847.

[61] L.P. Singh, C. Alba-Simionesco, R. Richert, Dynamics of glass-forming liquids. XVII. Dielectric relaxation and intermolecular association in a series of isomeric octyl alcohols, J. Chem. Phys. 139 (14) (Oct. 2013), 144503, https://doi.org/10.1063/1.4823998.

[62] J. Huo, et al., Molecular engineering of blue diphenylsulfone-based emitter with aggregation-enhanced emission and thermally activated delayed fluorescence characteristics: impairing intermolecular electron-exchange interactions using steric hindrance, Chem. Eng. J. 452 (Jan. 2023), 138957, https://doi.org/10.1016/j.cej.2022.138957.

[63] G. Cooke, V.M. Rotello, Methods of modulating hydrogen bonded interactions in synthetic host–guest systems, Chem. Soc. Rev. 31 (5) (2002) 275–286, https://doi.org/10.1039/B103906G.

[64] J. Mucelini, et al., Understanding the interplay between π–π and cation–π interactions in [janusene–Ag]$^+$ host–guest systems: a computational approach, Dalton Trans. 48 (35) (2019) 13281–13292, https://doi.org/10.1039/C9DT02307K.

[65] Y. Yoshimura, T. Takekiyo, H. Abe, N. Hamaya, High-pressure phase behavior of the room temperature ionic liquid 1-ethyl-3-methylimidazolium nitrate, J. Mol. Liq. 206 (Jun. 2015) 89–94, https://doi.org/10.1016/j.molliq.2015.02.010.